Available online at www.sciencedirect.com
SCIENCE DIRECT®
Biomaterials 25 (2004) 4947–4954
Biomaterials
www.elsevier.com/locate/biomaterials

Analysis of 3D bone ingrowth into polymer scaffolds via micro-computed tomography imaging

Anthony C. Jones[a], Bruce Milthorpe[b,*], Holger Averdunk[a], Ajay Limaye[c], Tim J. Senden[a], Arthur Sakellariou[a], Adrian P. Sheppard[a], Rob M. Sok[a], Mark A. Knackstedt[a], Arthur Brandwood[b], Dennis Rohner[d], Dietmar W. Hutmacher[e]

[a] *Department of Applied Mathematics, Research School of Physical Science and Engineering, Australian National University, Canberra ACT 0200, Australia*
[b] *University of New South Wales, Graduate School of Biomedical Engineering, Sydney, Australia*
[c] *VizLab, Supercomputing Facility, Australian National University Canberra ACT 0200, Australia*
[d] *Cranio-Facial-Center Hirslanden, CH-5000 Aarau, Switzerland*
[e] *Laboratory for Biomedical Engineering, Department of Engineering, National University of Singapore, 10 Kent Ridge Crescent, Singapore 119260, Singapore*

Received 14 January 2004; accepted 20 January 2004

Abstract

This paper illustrates the utility of micro-computed tomography (micro-CT) to study the process of tissue engineered bone growth. A micro-CT facility for imaging and visualising biomaterials in three dimensions (3D) is described. The facility is capable of acquiring 3D images made up of 2000^3 voxels on specimens up to 60 mm in extent with resolutions down to 2 μm. This allows the 3D structure of tissue engineered materials to be imaged across three orders of magnitude of detail. The capabilities of micro-CT are demonstrated by imaging the Haversian network within human femoral cortical bone (distal diaphysis) and bone ingrowth into a porous scaffold at varying resolutions. Phase identification combined with 3D visualisation enables one to observe the complex topology of the canalicular system of the cortical bone. Imaging of the tissue engineered bone at a scale of 1 cm and resolutions of 10 μm allows visualisation of the complex ingrowth of bone into the polymer scaffold. Further imaging at 2 μm resolution allows observation of bone ultra-structure. These observations illustrate the benefits of tomography over traditional techniques for the characterisation of bone morphology and interconnectivity and performs a complimentary role to current histomorphometric techniques.

Keywords: Image analysis; Scaffold; Bone tissue engineering; Micro-structure; X-ray micro-computed tomography

1. Introduction

Tissue engineering is a rapidly emerging interdisciplinary research field that aims to develop alternative therapeutic strategies for repair and/or reconstruction of damaged or lost tissue and organs. Porous polymer scaffolds are promising materials for tissue engineering because they offer a physical, three-dimensional (3D) support and serve as a template for cell proliferation and ultimately tissue formation. The question of how to optimally design such a scaffold for different tissue remains unsolved. However, various bone engineering groups have noted a correlation of scaffold pore size with bone ingrowth [1,2]. Pore sizes of greater than 300 μm were observed to have a greater penetration of mineralised tissue in comparison with smaller pore sizes. At pore sizes of 75 μm, hardly any mineralised tissue was found within the scaffold. It is believed that for smaller pore sizes the penetration of neovascularisation, and hence nutrient supply, to the growing cells is hindered. Three-dimensional scaffolds for tissue engineering, to date, have also been found to be less than ideal for applications in bone replacement because they lack the mechanical strength which is an essential prerequisite for implantation. Clearly, there are several requirements in the design of scaffolds for tissue engineering. Many of these requirements are complex and not yet fully understood.

*Corresponding author.
E-mail address: b.milthorpe@unsw.edu.au (B. Milthorpe).

0142-9612/$ - see front matter © 2004 Elsevier Ltd. All rights reserved.
doi:10.1016/j.biomaterials.2004.01.047

It can be concluded from the literature and the authors' own research, that scaffolds designed for use in cell-based therapies to repair/regenerate bone should provide the following minimal requirements: (i) a three-dimensional (3D) and highly porous structure to support cell attachment, proliferation and extra-cellular matrix (ECM) production; (ii) an interconnected/permeable pore network to promote nutrient and waste exchange; (iii) a biocompatible and bioresorbable substrate with controllable degradation rates; (iv) a suitable surface chemistry for cell attachment, proliferation, and differentiation; (v) mechanical properties to support, or match, those of the tissues at the site of implantation; (vi) an architecture which promotes formation of the native anisotropic tissue structure; and (vii) a reproducible architecture of clinically relevant size and shape [3–5]. To date, most scaffolds reported for bone repair conform to only a few of these criteria [6].

Scaffold processing techniques used to date have often focused on the development of porous materials via fibre bonding, solvent casting, particulate leaching, membrane lamination, melt moulding, temperature-induced phase separation, and gas foaming [2,7]. The control over scaffold architecture using these fabrication techniques are often highly process driven, and not design driven. As a result, investigators have recently turned to rapid prototyping (RP) techniques for producing porous scaffolds for bone engineering applications [8].

While the engineering potential of various scaffold architectures is considerable, the ability to design and optimise structures is still very much ad hoc since local structure and mechanical/transport properties have not been measurable during tissue growth in vitro or in vivo. Traditional methods for evaluating osseointegration of tissue engineered scaffold/cell constructs are based on 2D histological and radiographical techniques and in rare cases mechanical testing. To further the development of optimal scaffold architectures and to characterise accurately the growth of bone into scaffolds requires a fast and non-destructive technique to characterise and measure the 3D properties of scaffold/tissue composites during growth.

1.1. Composites during growth in 3D

Micro-computed tomography is a technique that can be used to complement existing analysis techniques and can be used to image specimens at the micron scale non-destructively. Müller and Ruegsegger have investigated, and quantified, the architecture of cancellous bone using micro-CT [9–15]; studies by Ritman et al. [16–25] have investigated vascular networks and bone deposition rates using micro-CT; and other groups have investigated the effects of osteoarthritic disease upon bone structure [26–30].

There exists the clear potential for X-ray micro-CT techniques to study the process of tissue engineered bone growth in 3D. This paper describes the imaging and visualisation of the canalicular topology within human cortical bone to assess the regeneration of bone tissue in a pig orbit reconstruction explanted after a 3 month in vivo growth period. We hypothesised, based on the capabilities of the system, that imaging of bone and tissue engineered bone at a scale of 1 cm at resolutions of 10 μm allows one to visualise the complex ingrowth of bone into the polymer scaffold. Observations at this scale allow one to quantitatively assess the morphology and effectiveness of bone ingrowth at the scale of the full scaffold implant. At higher resolutions, voxel size close to 2 μm, micro-CT should enable one to image variations in mineralisation of the ingrowing bone.

2. Materials and methods

2.1. Micro-CT image acquisition

The experimental apparatus was developed and built at the Australian National University utilising a cone beam geometry (Fig. 1) [31]. By moving the position of the rotation stage and X-ray camera, magnifications can be set between x1.1 to over x100. The X-ray source generates a polychromatic beam via Bremsstrahlung, which is generally filtered to minimise beam hardening artifacts. The limiting resolution is between 2–5 μm and depends on the operating voltage (30–225 kV). The X-ray camera can acquire radiographs with up to 2048^2 pixels at a depth of 16 bits per pixel. The large range of X-ray energies is ideal for optimising the contrast between the different phases in biomaterials and the large dynamic range of the X-ray camera is ideal for collecting the data with a large signal-to-noise ratio. Combining these two important attributes allows one to generate high-contrast and low-noise images of the internal structure within biomaterials.

The maximum field of view (FOV) is 60 mm. Tomographic imaging is achieved by acquiring a series of radiographs at different viewing angles around 360°.

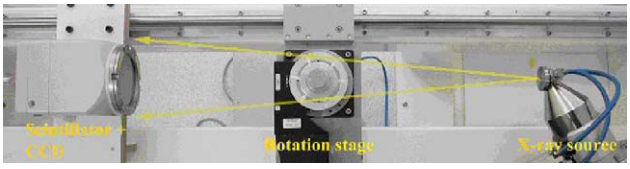

Fig. 1. X-ray micro-CT apparatus, with cone-beam geometry highlighted.

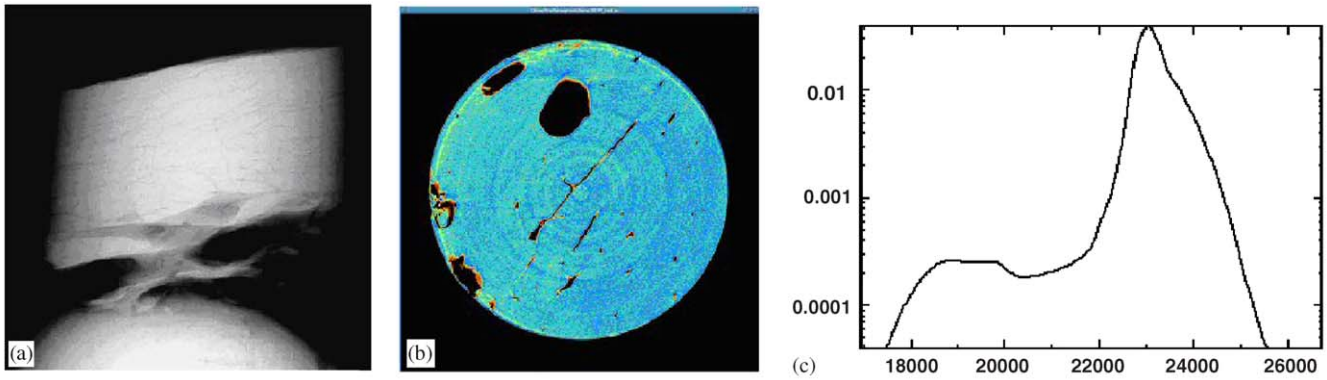

Fig. 2. (a) Single radiograph showing cortical bone specimen and mounting stub. (b) Central slice of tomogram showing channels within cortical bone. (c) Normalised intensity histogram of entire tomogram.

To sample optimally the specimen, the number of radiographs in a tomographic series is $\pi/2$ times the number of pixels in the width of the radiograph. An example of a single radiograph at 1024^2 of a 5 mm cylinder of mid-femoral cortical bone is shown in Fig. 2a. This image, taken at a magnification factor of $\times 11.9$, has a voxel size of 5.6 μm. A 2 mm thick plate was fabricated from human bone and was placed over the X-ray source to filter low energy X-rays. Whilst this led to a reduction in beam hardening artefacts, the reduced X-ray flux required a corresponding increase in acquisition time. The X-ray source was operated at a voltage of 80 kV and current of 180 μA. In total, 1600 projections were captured over 360°, resulting in 3.8 Gbytes of data. The entire acquisition took approximately 16 hours with an exposure time of 30 s/projection. For the 2048^3 voxel tomogram, 3000 projections were collected, resulting in 24 Gbytes of data collected in 30 hours.

2.2. Image reconstruction

The tomographic series are first pre-processed and then reconstructed with locally written software. The reconstruction is based on the Feldkamp algorithm [32]. All data are processed on an AlphaServer Supercomputer (see: http://nf.apac.edu.au/facilities/sc/hardware.php). It takes 1 hour to generate a 1024^3 voxel tomogram on 32 CPUs and 4 hours to generate a 2048^3 voxel tomogram on 128 CPUs. An example of the central slice through a cortical bone tomogram is shown in Fig. 2b. The tomogram has a voxel size of 5.6 μm and at this resolution non-mineralised channels with diameters of 10–50 μm are easily resolved.

2.3. Phase identification

Tomograms consist of a cubic array of voxels with "energy-averaged" attenuation values, normalised to 16-bit intensities. In Fig. 2c, we show the normalised intensity histogram generated from the cortical bone cylinder encompassing slightly less than 1 billion voxels. The histogram shows two distinct peaks—the peak with the lower value is associated with the non-mineralised channels, whilst the peak with the large value is associated with the mineralised phase.

One would wish to have a clear bimodal distribution between the pore and mineralised phase peaks. Unfortunately, the presence of features (e.g., osteocytes, cement lines and micro-cracks) in the mineralised phase at scales smaller than the voxel resolution and a significant number of bone/pore interface voxels lead to a spread in the histogram. This makes it difficult to differentiate the two phases unambiguously. To analyse tomograms quantitatively, it is necessary to have a well defined and consistent method to label each voxel as either pore or mineralised phase. The simplest method is to choose a global threshold value. In practice, this is not the best method, due to the amount of peak overlap in the intensity histogram.

It has been shown that a reliable method of phase separation can be made through detection and localisation of edges between distinct phases. We use an edge-based kriging segmentation algorithm [33] to define the binary pore-solid image. This approach involves the choice of 2 cutoff values lying near the two peaks; everything below the lower cutoff is designated as pore, and everything above the upper cuttoff is designated solid. For the cortical bone we observe the pore phase peak at 19,800 and the mineralised phase peak at 23,000. We chose cutoff thresholds of 20,000 and 22,000, respectively. Indicator kriging [32] is then performed to define the interface between the phases.

While cortical bone structure leads to the differentiation of two phases, in many cases one may wish to differentiate multiple phases. In the latter sections, we describe the phase separation of the tissue engineered bone into three phases; strongly mineralised phase, polymer scaffold and poorly mineralised/pore phase.

Fig. 3. 3D Visualisation of the topology of Haversian/Volkmann channels within human cortical bone.

2.4. 3D Visualisation

Volume rendering is a 3D visualisation method wherein the data volume is rendered directly without decomposing it into geometric primitives. Typically the attenuation values within the volume is assigned a colour and transparency depending upon lookup tables, rays are traced into the volume and they are attenuated and coloured depending on the transparency of their route through the volume. We have used a 2 GHz Pentium 4 with 1 Gb RAM to generate movies illustrating the distribution of phases in 3D. Custom built scripts along with commercial software, Houdini (www.sidefx.com) and Renderman (www.pixar.com), are used in the rendering process. Typical rendering time is about 60 s per image frame. Fig. 3 shows a frame from a 3D visualisation of the cannicular network within the cylindrical section of the femoral bone. The upper part corresponds to the endosteal or marrow surface. The cannicular network is highly anisotropic, the alignment of the channels coinciding with the long axis of the bone. Larger channels (presumed to be Haversian canals) are connected to the endosteal surface by smaller, more tortuous channels, presumably Volkmann canals. Full 3D movies are available for download at the following URL: http://www.rsphysse.anu.edu.au/appmaths/ct_movies.

2.5. Preparation and implantation of polymer scaffolds

The scaffold design considered in this paper was fabricated at the Laboratory of Biomedical Engineering, National University of Singapore [34] using a rapid prototyping technique known as fused deposition modelling (FDM). Ten pigs were anaesthetised and a defect measuring 1.5×2.5 cm was created in the medial wall of each orbit. A mould was taken of the defect using silicon rubber and the wound was sutured shut. A negative mould was then taken using dental cement and a PCL scaffold sheet was heated and pressed to fit the mould. The wound was left for 3–7 days to simulate typical human clinical experience, after which the wound was reopened and one of four protocols assigned. Group one were left as control; group two a graft of PLLA/PDLA non-porous sheeting was implanted; group three were assigned moulded PCL scaffolds; and group four were assigned porous PCL scaffolds that were bathed in a solution of the animals marrow aspirate for thirty minutes prior to implantation.

After 3 months of healing, all grafts specimens were extracted, fixed in buffered formalin, air-dried and analysed with micro-CT. In this paper, we present only the data from group four. Other comparative studies have been published on this data set [35].

3. Results

3.1. Scaffold/tissue construct

The tissue engineered bone was first imaged at a magnification factor of $\times 7.14$, resulting in a voxel size of 9.4 μm. The bone filter was also used for this specimen. The X-ray source was operated at a voltage of 80 kV and current of 180 μA. In total, 1600 projections were captured over 360 degrees. The entire acquisition took approximately 16 h with an exposure time of 32 s per projection.

A set of representative slices from the reconstructed tomographic data is shown in Fig. 4, where the slices are 280 μm apart. Three phases are evident in the images; strongly mineralised (bright), polymer (intermediate) and poorly mineralised/pore phase (dark). The host bone is shown in the lower right corner of each slice. The PCL scaffold exhibits regular lattice-shaped struts, and appears to be encapsulated to some extent by fibrous tissue. A number of interesting features are evident. Signs of degradation are visible within the scaffold: cracks (A1), degradation of the PCL filaments from an original diameter of 500 μm to approx. 300 μm, and distortion (bending) of the regular structure (A2). We also observe a large region of strongly mineralised phase within the scaffold (B), but this phase lies away from the host bone. Little bone ingrowth into the scaffold from the host bone is noted.

It is unclear from these images whether the bone within the scaffold is connected to the host bone. This raises a question about the direction of the mineralising

front. Is the observed tissue ingrowth from the host bone, or rather 'outgrowth' from the marrow aspirate cells?

As expected, the architecture of the bone is defined by the scaffold, giving it a regular lattice structure. Regions of soft tissue ingrowth (C) are observed within the scaffold. The apparent structure, lines of material almost as dense as the polymer, is presumably associated with artefacts from the dehydration process.

The normalised intensity histogram is given in Fig. 5. The peaks in the phases are observed at 6100 (pore), 7800 (polymer) and 12800 (mineralised tissue). To differentiate the image into the three separate phases we perform two phase-separation steps; between the void and solid phases, and between the polymer and mineralised bone phases. In the former case we choose cut-off thresholds of 6800 and 7250 and in the latter case, thresholds of 10,000 and 12,000. Indicator kriging is then performed to define the boundaries of the phases. Fig. 5 shows the separation of voxels into 3 phases by application of the segmentation algorithm twice. An example of the original grey scale image and the resultant phase separated results are given in Fig. 6.

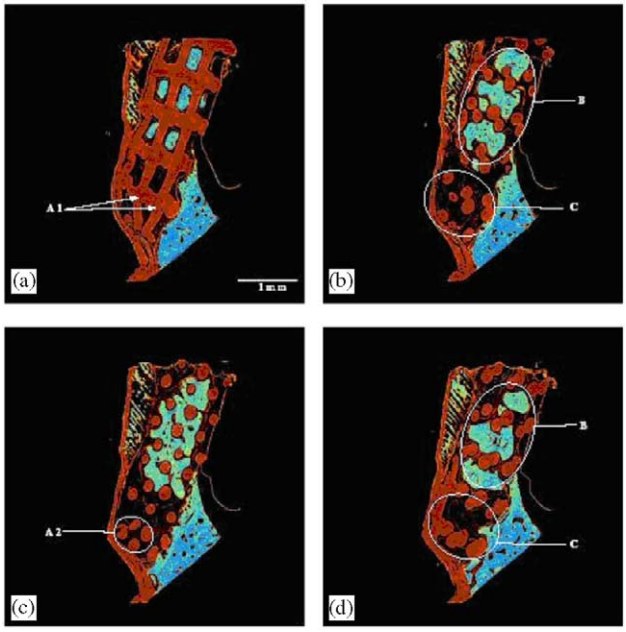

Fig. 4. Slices of PCL scaffold + marrow tomogram, 280 μm apart. A1: cracks in scaffold; A2: distortion of the regular polymer microstructure; B: mineralised phase within scaffold; C: area of soft tissue ingrowth only.

After phase separation we generate 3D visualisations of the distribution of polymer and mineralised phase within the specimen. A number of frames from this visualisation are shown in Fig. 7. Investigation of the 3D structure leads to further information about the process of bone ingrowth. Firstly we note that the bone ingrowth follows a strongly preferred orientation; the original scaffold was generated using a 0/60/120 degree pattern in the FDM process [34]. The growth of the bone was strongly oriented along the plane of fabrication. In Fig. 7(b) and (c) it is also observed that the bone ingrowth is primarily isolated to a single slice within the scaffold, on average $\sim$400 μm thick perpendicular to the fabrication plane. In contrast, the growth within the plane of fabrication extends $\sim$3 and $\sim$1.4 mm. It is unclear why the preferred orientation is observed, as pore sizes are comparable along all three directions within the scaffold. One can again observe in 3D the bending of polymer struts near the host bone due to the ingrowth into the pores nearest the host bone interface (Fig. 7a).

Three-dimensional imaging allows one to investigate the potential connectivity between the host bone and the bone ingrowth within the scaffold. To do this we zoom in near the host/implant interface. The image in Fig. 8 indicates that the large region of bone ingrowth in the scaffold is disconnected from the host bone even though it is very close to the host bone in one region. This lack

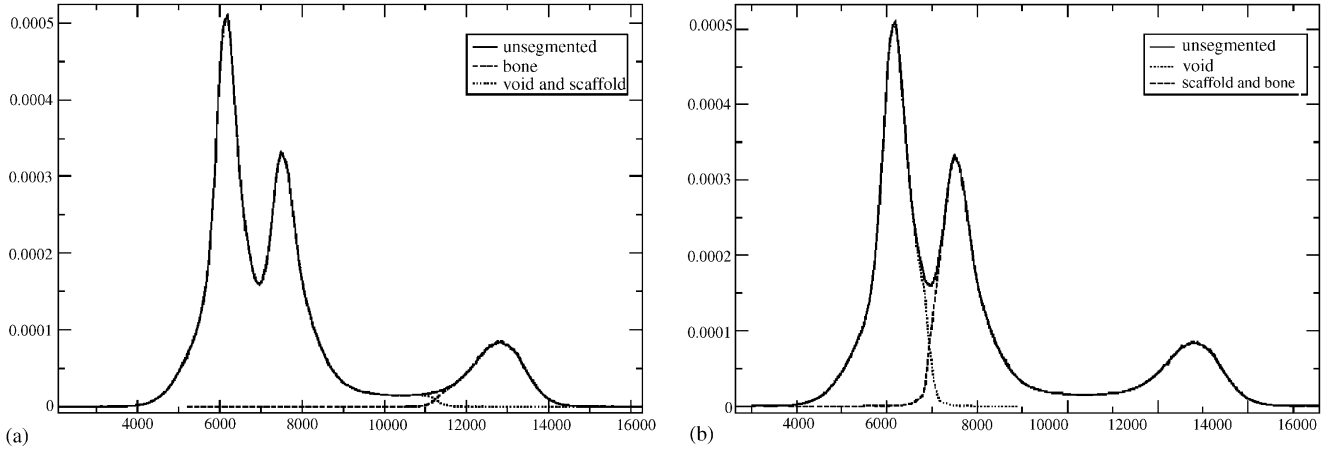

Fig. 5. Normalised intensity histograms, showing the result of two applications of the segmentation algorithm; (a) represents the first segmentation between bone and polymer/pore; (b) represents the second segmentation between pore and polymer/bone voxels.

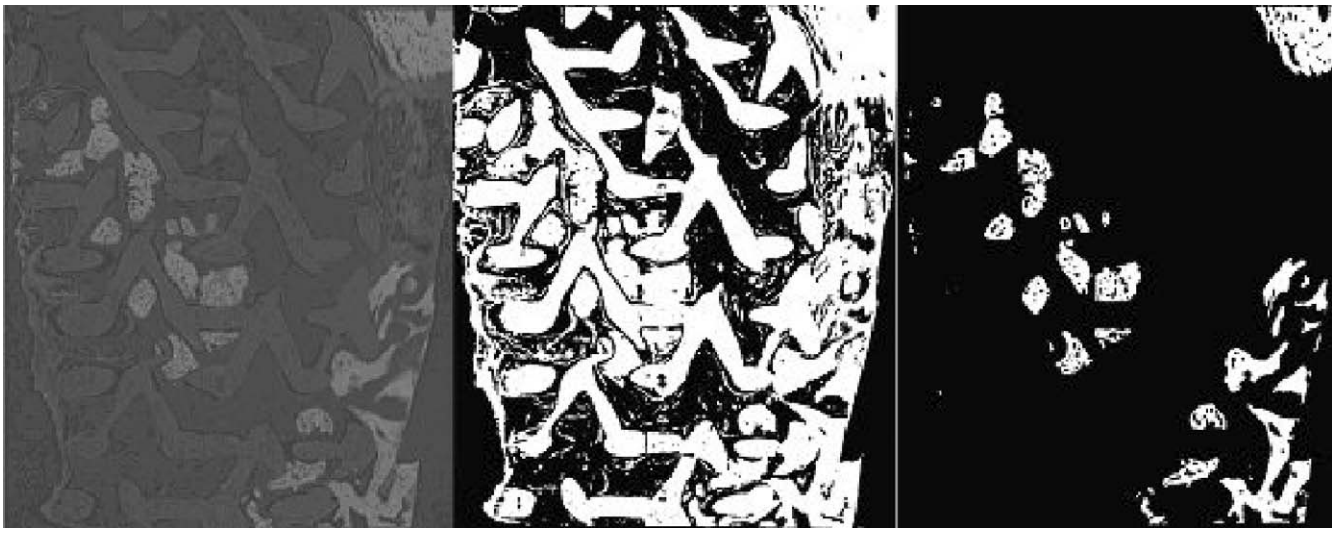

Fig. 6. Slice of PCL graft tomogram illustrating segmentation; grey level image (left); bone and scaffold (middle); and bone (right).

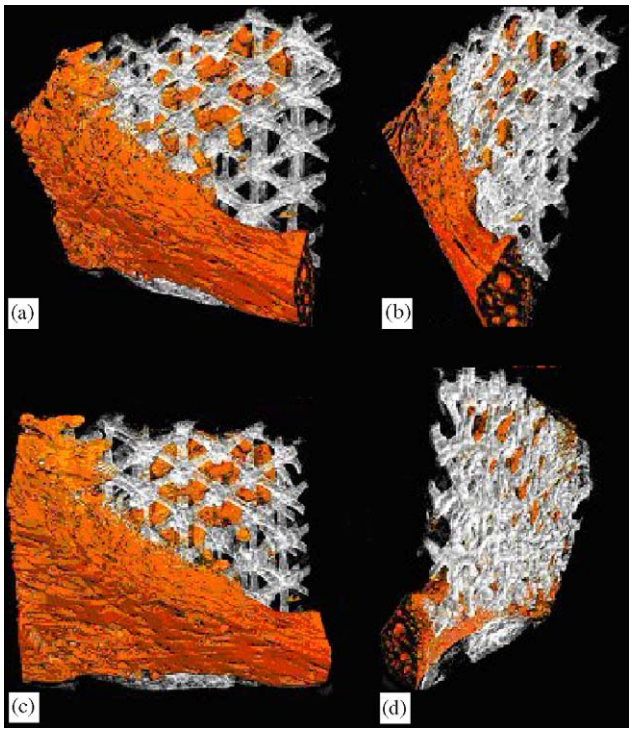

Fig. 7. 3D Renderings of PCL graft data set at different rotations.

of connection to the host bone is of considerable interest in determining mechanisms of bone regeneration using tissue engineering techniques.

3.2. Higher resolution imaging

A number of features could not be visualised within the bone at the resolution described above. This led to a study of subsets of the original system at higher resolutions. In particular, we wished to image a region of the bone ingrowth at higher resolutions.

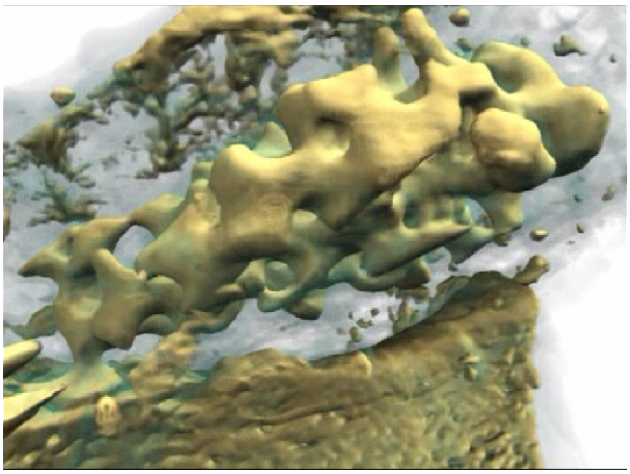

Fig. 8. Image from 3D data set showing non-conjunction of new bone, in scaffold, to old bone (lower left).

A 2 mm cubed specimen was taken from the mineralised phase within the scaffold and was imaged with 2048^3 voxels at a voxel size of 1.6 μm. Fig. 9 is a subvolume of the data set which shows the surfaces of mineralisation. Apart from the polymer scaffold, internal substructure can be observed. At the moment it is not possible to identify these substructures with certainty, although blood vessels and larger cells would certainly contribute.

4. Discussion

The utility of micro-CT is demonstrated by the ability to obtain relationships even at relatively coarse resolutions, as shown in the rendering of the canalicular structures in cortical bone (Fig. 3, see URL for animation). From the animation the anisotropy of the

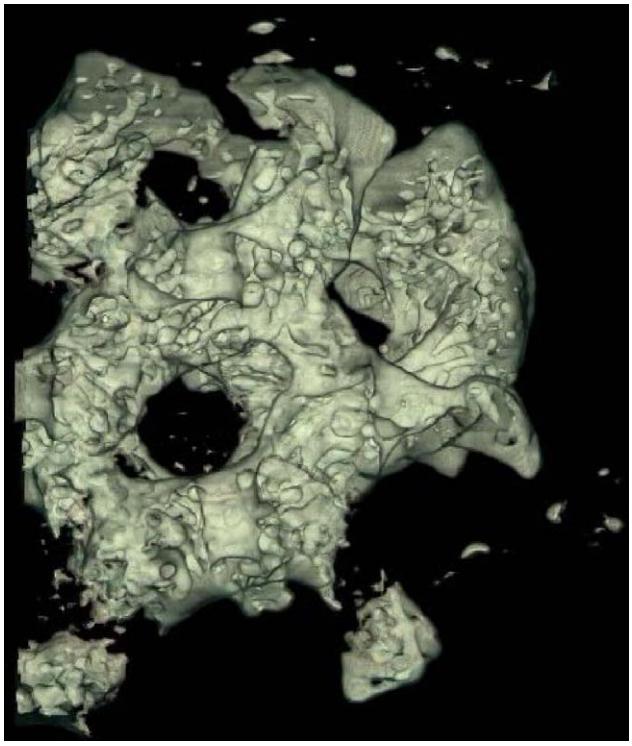

Fig. 9. Very high resolution 3D data set of regenerating bone within scaffold showing substructure within calcified tissue.

main canals is obvious. The relationships between the Haversian and Volkmann canals, including the bending of the Volkmann canals near the periosteal surface provide details that are not readily visible from standard 2D histological imaging. Examination of the animation for the ingrowth of calcifying tissue into a scaffold reveals several significant features (Fig. 7). There are sharp and distinct edges to the calcifying tissue. The process of calcification would appear to be one where the process of calcification is very rapid, once the signal to calcify has occured. The lack of graded edges could signify that calcification is a spatially abrupt process.

The nonunion between mineralising tissue in the scaffold and the host bone occurs primarily on an original surface. A surface created during surgery shows good reconnection. One reason for this difference might be that the biological potential was limited on the original surface as only a bone marrow coating was possible due to the clinical requirements explained above. It would be instructive to use a true cell bone MSC seeding and culturing technique to establish the connection. This observation has significance from the point of view of general bone regeneration versus wound healing. A wound would appear to be necessary for outgrowth and in particular for the bonding of tissue engineered bone.

At the highest resolution, $\sim 2\,\mu m$ voxels, imaging allows the visualisation of the sub-structure of calcifying tissue/callus. This area requires much more investigation to make serious physiological assignment to the various sub-structures. The current 2 mm field of view does not present a limitation for these high resolution studies, indeed as three orders in length scale are feasible mechanical properties [36] and transport modeling [37] are still meaningful. Apart from these analyses number of morphological measures are being investigated, such as; volume fractions of tissues, directivity of calcifying tissue, porosity, pore connectivity, putative vascularisation, curvature and surface-to-volume measures (Mincowski measures [38]). Initially these measurements will be used at correlators for the processes of tissue healing and regeneration within the scaffold environment.

5. Conclusion

Clearly, in a structure as complex as bone, micro-CT provides a distinct advantage over conventional microscopy. Structures can be followed continuously from the level of osteon through to gross bone morphology. It is not difficult to imagine that micro-CT will become a standard technique in the assessment of tissue engineered bone, bone regeneration and bone bonding. Several challenges remain for the technique, however. Developments in instrumentation need focus more on the discrimination of different tissue types than on improvements to spatial resolution. Although visualization has become very sophisticated, the 3D analytical tools and measures are still under development and will require a substantial effort before they are refined to the point of everyday use. However, this said the interdisciplinary nature of bone research affords the great possibility for exchange with many other materials sciences in which these issues too are currently under serious consideration.

Acknowledgements

This project was supported in part by grants from the Australian Research Council (ARC, DP0345886), and the National University of Singapore. Milthorpe, Knackstedt and Hutmacher acknowledge the support of the Australian Research Council under Project DP0345886, A10007257 and A10007207. Hutmacher acknowledges the support of the National University of Singapore (NUS Young Investigator Grant WBS 397 000 003 650). Senden gratefully acknowledges the ARC for his Fellowship. Knackstedt acknowledges the Australian Partnership for Advanced Computing (APAC) for financial support through their expertise program. We thank APAC and the ANU Supercomputing Facility for generous allocations of computer time.

References

[1] Taboas JM, Maddox RD, Krebsbach PH, Hollister SJ. Indirect solid free form fabrication of local and global porous, biomimetic and composite 3D polymer-ceramic scaffolds. Biomaterials 2003;24:181–94.

[2] Marra KG, Szem JW, Kumta PN, DiMilla PA, Weiss LE. In vitro analysis of biodegradable polymer blend/hydroxyapatite composites for bone tissue engineering. J Biomed Mater Rel Res 1999;47:324–35.

[3] Hollister SJ, Maddox RD, Taboas JM. Optimal design and fabrication of scaffolds to mimic tissue properties and satisfy biological contraints. Biomaterials 2002;23:4095–103.

[4] Hutmacher DW. Scaffolds in tissue engineering bone and cartilage. Biomaterials 2000;21:2529–43.

[5] Landers R, Mülhaupt R. Desktop manufacturing of complex objects, prototypes & biomedical scaffolds by means of computer-assisted design combined with computer-guided 3D plotting of polymers & reactive oligomers. Macromol Mater Eng 2000; 282:17–21.

[6] Kim SS, Utsunomiya H, Koski JA, Wu BM, Cima MJ, Sohn J, Griffith LG, Vacanti JP. Survival and function of hepatocytes on a novel three-dimensional synthetic biodegradable polymer scaffold with an intrinsic network of channels. Ann Surg 1998; 228:8–13.

[7] Lill CA, Gerlach UV, Eckhardt C, Goldhahn J, Schneider E. Bone changes due to glucocorticoid application in an ovariectomized animal model for fracture treatment in osteoporosis. Osteoporosis Int 2002;13:407–14.

[8] Yang S, Leong K-F, Du Z, Chua C-K. Review: the design of scaffolds for use in tissue engineering. Part II. Rapid prototyping techniques. Tissue Eng 2002;8:1–12.

[9] Müller R. Non-invasive bone biopsy: a new method to analyse and display the 3D structure of trabecular bone. Phys Med Biol 1994;39:145–64.

[10] Müller R, Hahn M, Vogel M, Delling G, Rüegsegge Pr. Morphometric analysis of non-invasively assessed bone biopsies: comparison of high-resolution computed tomography and histologic sections. Bone 1996;18:215–20.

[11] Müller R, Hildebrand T, Hauselmann HJ, Rüegsegger P. Resolution dependency of micro-structural properties of cancellous bone based on 3d-microct. Technol Health Care 1996;4:113–9.

[12] Müller R, Rüegsegger P. Three dimensional finite element modelling of non-invasively assessed trabecular bone structures. Med Eng Phys 1995;17:126–33.

[13] Müller R, van Campenhout H, van Damme B, van der Perre G, Dequeker J, Hildebrand T, Rüegsegger P. Morphometric analysis of human bone biopsies: a quantitative structural comparison of histological sections and micro-computed tomography. Bone 1998;23:59–66.

[14] Rüegsegger P. Imaging of bone structure, 2nd ed. Boca Raton: CRC Press; 2001. p. 1–24 [Chapter 9].

[15] Rüegsegger P, Koller B, Müller R. A microtomographic system for nondestructive evaluation of bone architecture. Calcified Tissue Int 1996;58:24–9.

[16] Bentley MD, Ortiz MC, Ritman EL, Romero C. The use of Microcomputed tomography to study microvasculature in small rodents. Am J Physiol—Reg Integ Comp Physiol 2002;282: 1267–79.

[17] Jorgensen SM, Demirkaya O, Ritman EL. Three-dimensional imaging of vasculature and parenchyma in intact rodent organs with X-ray micro-CT. Am J Physiol 1998;275:H1103–14.

[18] Martin EA, Ritman EL, Turner RT. Time course of epiphyseal growth plate fusion in rat tibiae. Bone 2003;32:261–7.

[19] Ortiz MC, Garcia-Sanz A, Bentley MD, Fortepiani LA, Garcia-Estan J, Ritman EL, Romero JC, Juncos LA. Microcomputed tomography of kidneys following chronic bile duct ligation. Kidney Int 2000;58:1632–40.

[20] Peyrin F, Salome M, Cloetens P, Laval-Jeantet AM, Ritman E, Rüegsegger P. Micro-CT examinations of trabecular bone samples at different resolutions: 14, 7 and 2 micron level. Technol Health Care 1998;6:391–401.

[21] Ritman EL. Molecular imaging in small animals - roles for micro-CT. J Cellular Biochem 2002;39:S116–24.

[22] Ritman EL, Bolander ME, Fitzpatrick LA, Turner RT. Micro-CT imaging of structure-to-function relationship of bone microstructure and associated vascular involvement. Technol Health Care 1998;6:403–12.

[23] Simopoulos DN, Gibbons SJ, Malysz J, Szurszewski JH, Farrugia G, Ritman EL, Moreland RB, Nehra A. Corporeal structural and vascular micro architecture with X-ray micro computerised tomography in normal and diabetic rabbits: histopathological correlation. J Urol 2002;165:1776–82.

[24] Wan S-Y, Kiraly AP, Ritman EI, Higgins WE. Extraction of the hepatic vasculature in rats using 3-D micro-CT images. IEEE Trans Med Imag 2000;19:964–71.

[25] Wan S-Y, Ritman EL, Higgins WE. Multi-generational analysis and visualization of the vascular tree in 3D micro-CT images. Comput Biol Med 2002;32:55–71.

[26] Dedrick DK, Goldstein SA, Brandt KD, O'Connor BL, Goulet RW, Albrecht M. A longitudinal study of subchondral plate and trabecular bone in cruciate-deficient dogs with osteoarthritis followed up for 54 months. Arthrit Rheum 1993;36:1460–7.

[27] Kinney JH, Ryaby JT, Haupt DL, Lane NE. Three-dimensional in vivo morphometry of trabecular bone in the ovx rat model of osteoporosis. Technol Health Care 1998;6:349–50.

[28] Lill CA, Fluegel AK, Schneider E. Effect of ovariectomy, malnutrition and glucocorticoid application on bone properties in sheep: a pilot study. Osteoporosis Int 2002;13:480–6.

[29] McLaughlin F, Mackintosh J, Hayes BP, McLaren A, Uings IJ, Salmon P, Humphreys J, Meldrum E, Farrow SN. Glucocorticoid-induced osteopenia in the mouse as assessed by histomorphometry, microcomputed tomography, and biochemical markers. Bone 2002;30:924–30.

[30] Nishida S, Tsurukami H, Sakai A, Sakata T, Ikeda S, Tanaka M, Ito M, Nakamura T. Stage-dependent changes in trabecular bone turnover and osteogenic capacity of marrow cells during development of type ii collagen-induced arthritis in mice. Bone 2002;30:872–9.

[31] Sakellariou A, Sawkins TJ, Limaye A. X-ray tomography for mesocale physics applications. Physica A, accepted for publication.

[32] Feldkamp LA, Davis LC, Kress JW. Practical cone-beam algorithm. J Opt Soc Am A 1984;1:612–9.

[33] Oh W, Lindquist WB. Image thresholding by indicator kriging. IEEE Trans Pattern Anal Mach Intell 1999;21:590–602.

[34] Zein I, Hutmacher DW, Tan KC, Teoh SH. Fused deposition modeling of novel scaffold architectures for tissue engineering applications. Biomaterials 2002;23:1169–85.

[35] Rohner D, Hutmacher DW, Tan KC, Oberholzer M, Hammer B. In-vivo efficacy of bone marrow-coated Polycaprolactone scaffolds for the reconstruction of orbital defects in the pig. J Biomed Mater Res Part B: Appl Biomater 2003;66B:574–80.

[36] Arns CH, Knackstedt MA, Pinczewski WV, Garboczi EJ. Computation of linear elastic properties from microtomographic images: methodology and agreement between theory and experiment. Geophysics 2002;67:1396–405.

[37] Arns CH, Knackstedt MA, Pinczewski WV, Lindquist WB. Accurate estimation of transport properties from microtomographic images. Geophysical Research Letters 2001;28:3361–4.

[38] Arns CH, Knackstedt MA, Mecke KR. Reconstructing complex materials via effective grain shapes. Physical Review Letters 2003;91:215506.